

Metalorganic Chemical Vapor Deposition of β -(Al_xGa_{1-x})₂O₃ thin films on (001) β -Ga₂O₃ substrates

A F M Anhar Uddin Bhuiyan^{1, a)}, Lingyu Meng¹, Hsien-Lien Huang², Jith Sarker³, Chris Chae²,
Baishakhi Mazumder³, Jinwoo Hwang², and Hongping Zhao^{1, 2, b)}

¹Department of Electrical and Computer Engineering, The Ohio State University, Columbus, OH 43210, USA

²Department of Materials Science and Engineering, The Ohio State University, Columbus, OH 43210, USA

³ Department of Materials Design and Innovation, University at Buffalo, Buffalo, New York 14260, USA

^{a)} Email: bhuiyan.13@osu.edu

^{b)} Corresponding author Email: zhao.2592@osu.edu

Abstract

Phase pure β -(Al_xGa_{1-x})₂O₃ thin films are grown on (001) oriented β -Ga₂O₃ substrates via metalorganic chemical vapor deposition (MOCVD). By systematically tuning the precursor molar flow rates, the epitaxial growth of coherently strained β -(Al_xGa_{1-x})₂O₃ films are demonstrated with up to 25% Al compositions as evaluated by high resolution x-ray diffraction (XRD). The asymmetrical reciprocal space mapping confirms the growth of coherent β -(Al_xGa_{1-x})₂O₃ films (x < 25%) on (001) β -Ga₂O₃ substrates. While the films show smooth surface morphologies, the alloy inhomogeneity with local segregation of Al along ($\bar{2}01$) plane is observed from atomic resolution STEM imaging, resulting in wavy and inhomogeneous interfaces in β -(Al_xGa_{1-x})₂O₃/ β -Ga₂O₃ superlattice structure. Room temperature Raman spectra of β -(Al_xGa_{1-x})₂O₃ films show similar characteristics peaks as (001) β -Ga₂O₃ substrate without obvious Raman shifts for films with different Al compositions. Atom probe tomography (APT) was used to investigate the atomic level structural chemistry with increasing Al content in the β -(Al_xGa_{1-x})₂O₃ films. A monotonous increase in chemical heterogeneity is observed from the in-plane Al/Ga distributions which was further confirmed via statistical frequency distribution analysis (FDA). Although the films exhibit

alloy fluctuations, n-type doping with good electrical properties are demonstrated for films with various Al compositions. The determined valence and conduction band offsets at β -(Al_xGa_{1-x})₂O₃/β-Ga₂O₃ heterojunctions using x-ray photoelectron spectroscopy (XPS) reveal the formation of type-II (staggered) band alignment.

Keywords: Ultra-wide bandgap, β -(Al_xGa_{1-x})₂O₃ alloy, (001) β-Ga₂O₃ substrates, metalorganic chemical vapor deposition (MOCVD), Bandgap engineering

I. Introduction

Aluminum gallium oxide ((Al_xGa_{1-x})₂O₃) with its tunable ultrawide bandgap energy (4.87 - 8.82 eV) [1] and high predicted breakdown field strength ($E_{Br} < 16$ MV/cm, $x < 0.8$) [2] has recently been emerged as a promising semiconducting material for next generation high power and high frequency electronic and ultraviolet optoelectronic applications. Considering its capability of controllable n-type doping [3], β -(Al_xGa_{1-x})₂O₃ based vertical power devices can gain benefits in terms of high breakdown field strength with higher Baliga's figure of merit (BFOM) for a variety of compositions [2], potentially exceeding that of Ga₂O₃. In addition, the formation of two-dimensional electron gas (2DEG) channel near the β -(Al_xGa_{1-x})₂O₃/Ga₂O₃ interfaces by modulation doping enhances the carrier density and electron mobility in lateral devices via the screening of the polar optical phonon scattering [4, 5]. A higher 2DEG charge can be achieved in the channel with enhanced mobility by increasing the Al content in β -(Al_xGa_{1-x})₂O₃ layer due to the increased conduction band offsets that facilitates better carrier confinement at β -(Al_xGa_{1-x})₂O₃/Ga₂O₃ heterointerfaces [6]. The recent demonstrations of high-performance modulation doped field-effect transistors (MODFETs) based on β -(Al_xGa_{1-x})₂O₃/Ga₂O₃ heterostructure [5, 7-8] have shown great promises of this material in applications such as integrated power and radio-frequency electronics.

Incorporating high Al composition in $(\text{Al}_x\text{Ga}_{1-x})_2\text{O}_3$ films are desired to achieve maximized mobility and high carrier density in lateral devices and high breakdown field strength in vertical power devices. However, the maximum Al incorporation in β - $(\text{Al}_x\text{Ga}_{1-x})_2\text{O}_3$ films are found to be limited due to the different ground state crystal structures of two parent materials: thermally stable monoclinic β - Ga_2O_3 (space group $C2/m$) and corundum α - Al_2O_3 (space group $R\bar{3}c$) [1]. Owing to its highly anisotropic crystalline structure, the epitaxial growth of monoclinic β - $(\text{Al}_x\text{Ga}_{1-x})_2\text{O}_3$ has been primarily established on (010) orientated β - Ga_2O_3 substrates with high quality and excellent electronic transport characteristics [9-13]. N-type doping of (010) β - $(\text{Al}_x\text{Ga}_{1-x})_2\text{O}_3$ films have been demonstrated using Si as dopant for a range of Al compositions [9, 10]. However, our previous studies have shown the appearance of γ -phase in MOCVD grown (010) oriented β - $(\text{Al}_x\text{Ga}_{1-x})_2\text{O}_3$ films while targeting for Al compositions above 27% [13], which impedes the pathway to achieve higher conduction band offsets at the interfaces between β - $(\text{Al}_x\text{Ga}_{1-x})_2\text{O}_3$ and β - Ga_2O_3 along (010) orientation. While achieving high Al composition (010) β - $(\text{Al}_x\text{Ga}_{1-x})_2\text{O}_3$ films were energetically unfavorable due to the structural phase transformation and domain rotation [13-17], we utilized other orientations of β - Ga_2O_3 substrates, such as (100) [18] and $(\bar{2}01)$ [19] for the growth of phase pure β - $(\text{Al}_x\text{Ga}_{1-x})_2\text{O}_3$ films by MOCVD growth methods, which exhibited Al incorporations up to < 52%. The band offsets determined at the β - $(\text{Al}_x\text{Ga}_{1-x})_2\text{O}_3/\text{Ga}_2\text{O}_3$ interfaces also exhibited a strong orientation dependence [20, 21]. The (100) oriented β - $(\text{Al}_x\text{Ga}_{1-x})_2\text{O}_3/\text{Ga}_2\text{O}_3$ heterointerfaces showed relatively larger conduction band offsets as compared to (010) and $(\bar{2}01)$ orientations for a wide range of Al compositions [21]. Although the high Al composition of β - $(\text{Al}_x\text{Ga}_{1-x})_2\text{O}_3$ films were achieved along (100) and $(\bar{2}01)$ orientations, the n-type doping in these films was found to be challenging due to the formation of incoherent boundary defects and alloy inhomogeneity in the films.

While the epitaxial growth of β -(Al_xGa_{1-x})₂O₃ have been extensively studied on (010), (100) and ($\bar{2}$ 01) orientated β -Ga₂O₃ substrates using MOCVD growth methods, the MOCVD epitaxial development of β -(Al_xGa_{1-x})₂O₃ films on (001) orientated β -Ga₂O₃ substrate is still lacking. The (001) oriented β -Ga₂O₃ substrates have been mostly utilized for the homoepitaxial growth of β -Ga₂O₃ films via halide vapor-phase epitaxy (HVPE) [22]. Majority of the existing vertical β -Ga₂O₃ devices based on Schottky barrier [23-25], p-n heterojunction [26], or metal-insulator-semiconductor (MIS) [27] diodes have been fabricated on (001) oriented β -Ga₂O₃ films. This indicates a great need for the development of high quality β -(Al_xGa_{1-x})₂O₃ films on (001) β -Ga₂O₃ substrates. Only recently, coherently strained (001) β -(Al_xGa_{1-x})₂O₃ films with up to 15% Al content have been demonstrated in molecular beam epitaxy (MBE) via metal oxide-catalyzed epitaxy using Sn as surfactant for β -(Al_xGa_{1-x})₂O₃ film growths [28]. However, the investigation of the solubility limit of (001) β -(Al_xGa_{1-x})₂O₃ films grown using MOCVD are still not reported. In addition, the band offset values at the (001) oriented β -(Al_xGa_{1-x})₂O₃/Ga₂O₃ interfaces are still lacking.

In this study, we investigated the MOCVD growth of β -(Al_xGa_{1-x})₂O₃ films and β -(Al_xGa_{1-x})₂O₃/Ga₂O₃ superlattice structures on (001) β -Ga₂O₃ substrates. The structural, electrical, chemical and surface morphological properties of MOCVD grown (001) β -(Al_xGa_{1-x})₂O₃ films are evaluated by comprehensive material characterization, including XRD, high resolution STEM, energy dispersive x-ray spectroscopy (EDX), XPS, atomic force microscopy (AFM), field emission scanning electron microscopy (FESEM), APT and Raman spectroscopy. Moreover, the evolution of the band offsets at (001) β -(Al_xGa_{1-x})₂O₃/Ga₂O₃ heterointerfaces with the variation of Al compositions is also investigated by XPS measurement.

II. Experimental Section

β -(Al_xGa_{1-x})₂O₃ thin films were grown on (001) Fe-doped semi-insulating β -Ga₂O₃ substrates (purchased from Novel Crystal Technology) by using Agnitron Agilis MOCVD reactor. Trimethylaluminum (TMAI) and Triethylgallium (TEGa) were used as Al and Ga precursors, respectively. Pure O₂ gas was used as O-precursor and Argon (Ar) was used as the carrier gas. The growth temperature and the chamber pressure were set at 880 °C and 20 Torr, respectively. The TEGa molar flow rate was fixed at 11.95 $\mu\text{mol min}^{-1}$, while the TMAI molar flow rate was adjusted from 0.15 to 0.91 $\mu\text{mol min}^{-1}$. The O₂ molar flow rate was set at 500 sccm. The substrates were first ex-situ cleaned by using solvents and then a high-temperature in-situ cleaning was performed under O₂ atmosphere for 5 mins at 920 °C prior to the initiation of the epitaxial growth.

The Al compositions, crystalline structure, film quality and strain were evaluated by XRD measurements using a Bruker D8 Discover with Cu K α radiation x-ray source ($\lambda = 1.5418 \text{ \AA}$). The surface morphology and surface roughness were characterized using FESEM (FEI Helios 600) and AFM (Bruker AXS Dimension Icon), respectively. Room temperature Raman spectroscopy was performed using a laser beam of 514 nm (Renishaw-Smiths Detection Combined Raman-IR Microprobe). An aberration-corrected Thermo Fisher Scientific Themis-Z scanning transmission electron microscopy was used to obtain high angle annular dark field (HAADF) STEM images and EDX spectral mapping. Film thicknesses were obtained from the cross-sectional FESEM using coloaded sapphire substrates and STEM HAADF images as well as from STEM-EDX elemental mapping profile of the films. XPS measurements were performed by using Kratos Axis Ultra X-ray photoelectron spectrometer with a monochromatized Al K α x-ray source ($E_{\text{photon}} = 1486.6 \text{ eV}$) to determine the Al compositions and bandgaps of β -(Al_xGa_{1-x})₂O₃ thin films. The valance and conduction band offsets were also determined by utilizing XPS with an energy resolution of 0.1 eV. APT specimens were prepared using standard lift-out and annular milling method [29]. To

protect the surface from any potential ion beam damage, a 50 nm thick nickel (Ni) layer was deposited on top of the sample via electron beam evaporation. The APT data acquisitions were conducted using a pulsed laser-assisted CAMECA LEAP 5000X HR system. The CAMECA's Integrated Visualization and Analysis Software (IVAS 3.8.6) was used for the tip reconstructions and analysis.

III. Results and Discussions

High resolution XRD measurements were used to probe the crystalline quality of the MOCVD grown epi-films. Figures 1(a)-(c) show the XRD ω - 2θ scans for (002) reflections of β - $(\text{Al}_x\text{Ga}_{1-x})_2\text{O}_3$ thin films grown on (001) β - Ga_2O_3 substrates. The films were grown using $[\text{TMAI}]/[\text{TEGa}+\text{TMAI}]$ molar flow rate ratios of 2.53%, 3.71% and 5.98% with the targeted thicknesses of 200 nm. The high intensity diffraction peak at $2\theta = 31.83^\circ$ originates from the (002) reflection of the β - Ga_2O_3 substrates. With the increase of $[\text{TMAI}]/[\text{TEGa}+\text{TMAI}]$ molar flow rate ratio from 2.53% to 5.98%, the diffraction peak corresponding to (002) β - $(\text{Al}_x\text{Ga}_{1-x})_2\text{O}_3$ shifts toward higher 2θ angles due to the increase of the lattice mismatch between substrate and epi-films. The Al content in β - $(\text{Al}_x\text{Ga}_{1-x})_2\text{O}_3$ films are determined by calculating the interplanar distance between β - Ga_2O_3 substrate and β - $(\text{Al}_x\text{Ga}_{1-x})_2\text{O}_3$ epi-film from the corresponding XRD peak positions. The Al compositions of 11%, 14% and 25% are determined for $[\text{TMAI}]/[\text{TEGa}+\text{TMAI}]$ molar flow rate ratios of 2.53%, 3.71% and 5.98%, respectively. The Al compositions estimated from the interplanar distances between the substrate and epilayers are found to be in good agreement with the Al compositions estimated by assuming fully strained thin films growths on β - Ga_2O_3 substrate [28]. As the Al composition increases, β - $(\text{Al}_x\text{Ga}_{1-x})_2\text{O}_3$ peak intensity reduces, indicating the degradation of crystalline quality of the films with higher Al

compositions. However, the lower x-ray scattering factor of Al as compared to that of Ga atom may also partially contribute to the reduction of the peak intensity of β -(Al_xGa_{1-x})₂O₃ films with higher Al contents [30].

To investigate the strain state and confirm the coherent growth of (001) β -(Al_xGa_{1-x})₂O₃ films on β -Ga₂O₃ substrates, the asymmetrical reciprocal space mapping (RSM) was performed on β -(Al_xGa_{1-x})₂O₃ films for different Al compositions. Figures 1 (d)-(f) show the asymmetrical RSMs for ($\bar{2}04$) reflections of β -(Al_xGa_{1-x})₂O₃ films with 11%, 14%, and 25% Al compositions. The fully relaxed and strained positions are shown by the tilted and vertical black dashed lines, respectively. The maximum reflection intensity of ($\bar{2}04$) β -(Al_xGa_{1-x})₂O₃ reciprocal lattice point moves far from ($\bar{2}04$) β -Ga₂O₃ substrate peak as the Al composition increases along the fully strained vertical line, indicating the growth of fully coherent β -(Al_xGa_{1-x})₂O₃ films on (001) β -Ga₂O₃ substrates for different Al composition. The shifting of the peak position of ($\bar{2}04$) β -(Al_xGa_{1-x})₂O₃ towards higher Q_z values (out-of-plane reciprocal space lattice constant) due to higher Al incorporation indicates the increase of the lattice mismatch between the strained epi-films and substrates. The surface morphology and roughness of β -(Al_xGa_{1-x})₂O₃ films for a representative sample with Al composition of 14% are shown in Figure 2. Smooth and uniform surface morphologies with RMS roughness of 2.88 nm are measured from the FESEM and AFM images as shown in Figures 2(a) and (b), respectively.

Room temperature Raman spectra of the β -(Al_xGa_{1-x})₂O₃ films with different Al compositions are shown in Figure 3. The Raman spectrum of a single crystal (001) β -Ga₂O₃ bare substrate is also included in the figure as reference. In general, the irreducible representation for acoustical and optical zone center modes based on the factor group analysis [31] at the Γ point is $\Gamma_{\text{aco}} = A_u + 2B_u$ and $\Gamma_{\text{opt}} = 10A_g + 5B_g + 4A_u + 8B_u$, respectively. For the optical modes, A_g and B_g

are Raman active, while A_u and B_u modes are infrared active. Both A_g and B_g mode peaks are selectively observed in the Raman spectra of the (001) β - $(Al_xGa_{1-x})_2O_3$ films with different Al compositions, as shown in Figure 3. Ten Raman peaks are observed from both (001) β - Ga_2O_3 bare substrate and β - $(Al_xGa_{1-x})_2O_3$ films. Our experimental Raman mode frequencies correspond well with those reported in the literatures based on experimental and theoretical studies on (001) β - Ga_2O_3 [32, 33]. The peaks at around 169.6, 199.49, 319.8, 345.7, 416.2, 474.3, 629.4 and 765.5 cm^{-1} belong to the A_g vibrational mode and the peaks at around 144.9 and 651.2 cm^{-1} can be assigned to the B_g mode. These Raman-active modes can be classified into three groups: the high-frequency (770-500 cm^{-1}) stretching and bending of GaO_4 tetrahedra ($A_g^{(8)}$, $B_g^{(5)}$ and $A_g^{(10)}$), the mid-frequency (480-310 cm^{-1}) deformation of Ga_2O_6 octahedra ($A_g^{(4)}$ - $A_g^{(7)}$), and the low-frequency (below 200 cm^{-1}) libration and translation of tetrahedra–octahedra chains ($B_g^{(2)}$, $A_g^{(2)}$ and $A_g^{(3)}$) [34]. The Raman spectra of β - $(Al_xGa_{1-x})_2O_3$ films exhibit similar characteristics of spectrum of the bare β - Ga_2O_3 substrate, without any noticeable Raman shifts for different Al compositions, indicating that the symmetry of the β - $(Al_xGa_{1-x})_2O_3$ crystal structures is well maintained.

In order to investigate the crystalline properties of the materials grown on (001) β - Ga_2O_3 substrates, β - $(Al_xGa_{1-x})_2O_3$ thin film and β - $(Al_xGa_{1-x})_2O_3/Ga_2O_3$ superlattice (SL) structure are characterized using high-resolution STEM imaging. Figures 4(a)-(b) show the cross sectional HAADF-STEM images of the β - $(Al_xGa_{1-x})_2O_3$ film with a targeted 14% Al composition. Undisturbed monoclinic β -phase structures without noticeable phase transformation are observed from the STEM images. The sharp contrasts between the (001) β - Ga_2O_3 substrate (bright) and β - $(Al_xGa_{1-x})_2O_3$ epi-films (dark) indicate high quality interface. At the interface, the film displays a \sim 17 nm thick uniform cross section of β - $(Al_xGa_{1-x})_2O_3$ layer with homogeneous Al distribution.

However, as the growth continues, the compositional segregation with domain rotations is observed, as indicated by the strong tilted contrast in the epitaxial layer as shown in Figure 4(a). This significant contrast can also be seen at the atomic resolution image in Figure 4(b), where the non-uniform Al distribution causes fluctuations in atomic column intensity. The Al distribution patterns as indicated by the tilted darker contrast are found to align along the $(\bar{2}01)$ plane, which belongs to the crystal planes having the relatively low surface free energies. Our previous growth studies have shown high-Al incorporation (up to 48%) in β - $(\text{Al}_x\text{Ga}_{1-x})_2\text{O}_3$ films grown along $(\bar{2}01)$ orientation [19], indicating the strong preference of Al incorporation along $(\bar{2}01)$ plane, which can be related to its significantly lower surface free energy [35]. Such strong anisotropic characteristics of the β -gallia structure leads to the directional dependence of the Al distribution along $(\bar{2}01)$ plane in β - $(\text{Al}_x\text{Ga}_{1-x})_2\text{O}_3$ thin films grown on (001) β - $(\text{Al}_x\text{Ga}_{1-x})_2\text{O}_3$ substrates.

Additionally, in order to evaluate the compositional homogeneity and Al composition, STEM-EDX mapping was performed throughout the β - $(\text{Al}_x\text{Ga}_{1-x})_2\text{O}_3$ layer grown with 14% Al composition as shown in Figure 5. The EDX color maps of Ga (green) and Al (blue) elements in Figures 5(b)-(c) reveal the compositional segregation of the films, as also observed from the HAADF STEM images in Figure 4. The Al distribution pattern in the film along $(\bar{2}01)$ plane is also confirmed from the EDX color maps of Ga and Al atoms. The average Al compositions ($x = \sim 16.4\%$) estimated from the STEM-EDX elemental maps in Figure 5(e) matches well with those extracted from the XRD measurements ($x = 14\%$). Slightly higher Al compositions extracted from EDX elemental mapping can be due to the nonuniformity of the Al distribution in the films. In order to quantitatively evaluate the Al composition in the film along $(\bar{2}01)$ plane, we also performed the STEM-EDX mapping, focusing on the region that exhibits inhomogeneous Al distribution as shown in Figures 6 (a)-(e). The line scan as indicated by the orange arrow in Figure 6(a) provides

the concentration of each element, as shown in Figures 6(e). The quantitative EDX elemental mapping in Figure 6(e) confirms Al segregation along ($\bar{2}01$) plane with high Al content of 50% as indicated by the tilted darker contrast in the HAADF STEM images in Figure 6(a). However, Al composition of $\sim 13\%$ is extracted from the elemental mapping in Figure 6(e) from other regions of the films that exhibit compositional homogeneity and uniformity. While the compositional segregation is observed in the films due to the Al incorporation tendency along ($\bar{2}01$) plane, the first ~ 17 nm thick layer at the interfaces reveal homogenous Al distribution with good uniformity as shown in the darker contrast in the cross-sectional HAADF-STEM image in Figure 7 (a) and STEM-EDX elemental maps in Figures 7(b) - (e).

In addition to the growth of thin films, we also investigated the growth of β - $(\text{Al}_x\text{Ga}_{1-x})_2\text{O}_3$ / β - Ga_2O_3 superlattice structure grown with targeted Al compositions of 14% in the β - $(\text{Al}_x\text{Ga}_{1-x})_2\text{O}_3$ barrier layer. Figures 8 (a) and (b) show the cross sectional HAADF-STEM images for the SL structure at 100 nm and 20 nm scales, respectively. The SL structure is grown on a 65 nm thick β - Ga_2O_3 buffer layer. The darker contrast represents the β - $(\text{Al}_x\text{Ga}_{1-x})_2\text{O}_3$ barrier, while the brighter contrast corresponds to the β - Ga_2O_3 well layer. The growth of 8 periods of alternating SLs, maintaining the β -phase throughout the entire structure, is confirmed by the STEM images. However, due to the nonuniformity of the Al distribution in the film, β - $(\text{Al}_x\text{Ga}_{1-x})_2\text{O}_3$ layers show zigzag shapes with wavy and inhomogeneous interfaces between β - $(\text{Al}_x\text{Ga}_{1-x})_2\text{O}_3$ and β - Ga_2O_3 layers throughout the SL structure. The similar nonuniform structures are also observed from the STEM-EDX maps of the corresponding SL structures as shown in Figures 9 (a)-(e). The quantitative elemental mapping in Figure 9 (e) shows alternating compositional profiles of the periodic structures with around 12% Al incorporation in the β - $(\text{Al}_x\text{Ga}_{1-x})_2\text{O}_3$ layers.

APT was used to investigate the atomic scale chemical homogeneity in β -(Al_xGa_{1-x})₂O₃ layers with different Al content. Figure 10 shows the 3D elemental distribution of a β -(Al_xGa_{1-x})₂O₃ stack grown by varying the TMAI flow rate from 1 to 6 SCCM as shown in the schematic in Figure 10 (a). The red and blue dots correspond to the Al and Ga atoms, respectively. As growth continues, the density of the red dots increases with the increase of TMAI flow, indicating an increase in the Al contents. Our previous studies on MOCVD epitaxial growth of (010) oriented β -(Al_xGa_{1-x})₂O₃ thin films have shown excellent alloy homogeneity for the layers grown with relatively low Al compositions ($x < 27\%$), while chemical segregation was observed due to higher Al incorporation [13]. However, in the case of epitaxial growth of (001) oriented β -(Al_xGa_{1-x})₂O₃ thin films, we observed nonuniformity in the Al distribution even for low Al content layers as shown in the elemental mapping in Figure 10 (c), implying a strong dependence of the chemical inhomogeneity in β -(Al_xGa_{1-x})₂O₃ on the orientations of β -Ga₂O₃ substrates. While nonuniformity in the Al distribution is observed, the average Al compositions from APT are found to be consistent with the values determined from XRD and STEM-EDX mapping.

Additionally, in order to investigate the fluctuation in alloy homogeneity with increasing Al content in the layer, APT was also utilized to perform lateral Al/Ga distributions and frequency distribution analysis (FDA) of each corresponding layers as shown in the schematic in Figure 10(a). Figure 11 (a)-(f) show the in-plane Al/Ga ratio for different layers of β -(Al_xGa_{1-x})₂O₃ with increasing Al contents. From each layer, an analysis volume with a diameter of 80 nm and a thickness of 4 nm was chosen. With the increase of TMAI flow rate from 1 to 6 SCCM, the Al content in the layers increases as indicated by the increase of the Al/Ga ratio. The compositional inhomogeneity increases as the Al composition increases. The higher mobility of Ga adatoms on the growth surface leads to the lower compositional variation in lower Al content layers [36].

However, strong chemical heterogeneity is observed in the layer grown with higher TMAI flow rates, which can be due to the strong oxidization of Al adatoms [37] lowering the mobility of Al on growth surface. This compositional fluctuation in (001) β -(Al_xGa_{1-x})₂O₃ film can also be correlated with the STEM images as shown in Figure 5.

The Al distributions within each sub-layers with various TMAI flow rates were further evaluated by statistical FDA, as shown in Figures 12 (a)-(f), in order to statistically investigate the inhomogeneity in different layers with different Al content. In general, the chemical inhomogeneity in a layer is indicated by the deviation of the observed elemental distribution from that of a random binomial fitting. The value of Pearson coefficient, μ approaching towards 1 indicates statistically significant amount of elemental segregation and lower P-value provides higher confidence level during the null hypothesis testing [38]. For the lower TMAI flow rates, the observed Al distribution follows the expected binomial distribution, implying random distribution of Al atoms. However, the deviation between the observed Al distribution and random binomial fit increases with higher μ value, as the TMAI flow rates increase. This phenomenon indicates an increase in chemical inhomogeneity with the increase of Al content in the films as also observed from the in-plane Al/Ga lateral chemistry maps in Figure 11.

In addition to the investigation of the structural quality and chemical homogeneity, the band gaps of β -(Al_xGa_{1-x})₂O₃ thin films and the band offsets at β -(Al_xGa_{1-x})₂O₃/ β -Ga₂O₃ heterojunctions were also evaluated by using high resolution XPS. The determination of the bandgap energy using XPS technique by examining the onset of inelastic spectrum at the higher binding energy side of a strong intensity core level peak position is considered as a well-known method [39-42]. For the bandgap determination, Ga 2p_{3/2} core levels of both β -(Al_xGa_{1-x})₂O₃ and β -Ga₂O₃ thin films were used, as exemplarily shown in Figures 13 for β -(Al_xGa_{1-x})₂O₃ films with 25% Al composition. The

inset of the figure represents the zoomed view of the background region of Ga 2p_{3/2} core level. The intersection of the linear extrapolation of the loss spectra curve and the constant background is used to identify the onset of the inelastic loss spectra. From the difference between the onset of inelastic background and peak position of Ga 2p_{3/2} core level, the bandgaps of 4.88 eV, 5.04 eV and 5.15 eV are determined for β -Ga₂O₃ and β -(Al_xGa_{1-x})₂O₃ films with 11% and 25% Al compositions, respectively. The theoretically predicted bandgap values based on first-principles hybrid density functional theory (DFT) [1] matches well with the experimental bandgap energies obtained in this study by utilizing XPS.

The band offsets at β -(Al_xGa_{1-x})₂O₃/ β -Ga₂O₃ heterointerfaces are also determined using XPS for the Al compositions of 11% and 25%. Three types of samples were prepared for the band offset measurement: (a) 50 nm thick β -Ga₂O₃ film and (b) 200 nm thick β -(Al_xGa_{1-x})₂O₃ layers with 11% and 25% Al compositions, and (c) thin (2 nm) layer of β -(Al_xGa_{1-x})₂O₃ with x = 11% and 25% grown on 65 nm thick (001) β -Ga₂O₃ film for capturing all the electronic states from the heterointerfaces. The Kraut's method is employed for the determination of the valence (ΔE_v) band offsets as follows [43].

$$\Delta E_v = (E_{\text{Ga } 3d}^{\text{GaO}} - E_{\text{VBM}}^{\text{GaO}}) - (E_{\text{Al } 2p}^{\text{AlGaO}} - E_{\text{VBM}}^{\text{AlGaO}}) - (E_{\text{Ga } 3d}^{\text{AlGaO/GaO}} - E_{\text{Al } 2p}^{\text{AlGaO/GaO}}) \quad (1)$$

Using the extracted valence band offsets and bandgaps of β -Ga₂O₃ and β -(Al_xGa_{1-x})₂O₃ layers, the conduction band offsets (ΔE_c) at the β -(Al_xGa_{1-x})₂O₃/ β -Ga₂O₃ heterointerfaces are determined as follows:

$$\Delta E_c = E_g^{\text{AlGaO}} - E_g^{\text{GaO}} - \Delta E_v \quad (2)$$

Here, the binding energy corresponding to the valence band minimum (VBM) and Ga 3d core levels of 50 nm thick β -Ga₂O₃ films are defined as $E_{\text{VBM}}^{\text{GaO}}$ and $E_{\text{Ga } 3d}^{\text{GaO}}$, respectively. Similarly, $E_{\text{VBM}}^{\text{AlGaO}}$ and $E_{\text{Al } 2p}^{\text{AlGaO}}$ represent the VBM and the Al 2p core levels of 200 nm thick β -(Al_xGa_{1-x})₂O₃ layers.

The Ga 3d and Al 2p core levels of β -(Al_xGa_{1-x})₂O₃/β-Ga₂O₃ heterointerfaces are represented by $E_{\text{Ga } 3d}^{\text{AlGaO/GaO}}$ and $E_{\text{Al } 2p}^{\text{AlGaO/GaO}}$, respectively. The bandgaps of β-Ga₂O₃ and β-(Al_xGa_{1-x})₂O₃ are defined as E_g^{GaO} and E_g^{AlGaO} , respectively.

Figures 14 (a)-(c) show Ga 3d, Al 2p core levels and VBM of β-Ga₂O₃ and β-(Al_xGa_{1-x})₂O₃ layers as well as β-(Al_xGa_{1-x})₂O₃/β-Ga₂O₃ heterojunctions for 25% Al composition. After applying the Shirley background subtraction, the core level peak positions are calculated by fitting with Gaussian and Lorentzian line shapes. The valence band onsets are calculated by linearly extrapolating the leading edge to the background. Using equation (1), the ΔE_v of -0.04 and -0.08 eV are determined at β-(Al_xGa_{1-x})₂O₃/β-Ga₂O₃ interfaces with Al compositions of 11% and 25%, respectively. The corresponding ΔE_c of 0.17 and 0.35 eV are calculated using equation (2). The measured core-level binding energies, band gaps, valence and conduction band offsets for different Al compositions are summarized in Table 1. The heterointerfaces for both Al compositions show type-II (staggered) band alignment which is consistent with the theoretical DFT predictions for (001) orientation [44]. Previously, similar type-II band alignments were also observed at (010) and (100) β-(Al_xGa_{1-x})₂O₃/β-Ga₂O₃ interfaces, whereas ($\bar{2}01$) oriented β-(Al_xGa_{1-x})₂O₃/β-Ga₂O₃ exhibited type-I (straddling) band alignment [21].

The determined conduction band offsets at the interfaces between (001) β-Ga₂O₃ and β-(Al_xGa_{1-x})₂O₃ as a function of Al compositions are shown in Figure 15. The evolution of both experimentally and theoretically determined ΔE_c values as a function of Al compositions for differently oriented β-(Al_xGa_{1-x})₂O₃ films, such as (010), (100) and ($\bar{2}01$) are also included in the figure [20, 21]. The conduction band offsets exhibit a strong orientation dependence. For all orientations, the conduction band offsets are found to increase as the Al composition increases. However, among all the orientations, the (100) oriented β-(Al_xGa_{1-x})₂O₃/β-Ga₂O₃ interfaces show

highest conduction band offsets, which is in a good agreement with the theoretical DFT predictions [44].

Finally, the n-type conductivity of (001) β -(Al_xGa_{1-x})₂O₃ thin films for different Al compositions are also investigated by using Si as dopant. Figure 16 shows the room temperature Hall mobility vs. carrier concentration of Si doped (001) β -(Al_xGa_{1-x})₂O₃ films for different Al compositions. 200 nm thick β -(Al_xGa_{1-x})₂O₃ films with 11% Al compositions were grown with 0.53 nmole/min of silane flow rate and β -(Al_xGa_{1-x})₂O₃ films with 16% and 25% Al compositions were grown with silane flow of 3.1 nmole/min. All the films exhibit n-type conductivity with room temperature Hall mobility of 39-70 cm²/Vs and carrier concentrations ranging between 2 - 4 x 10¹⁷ cm⁻³. The results show decent electrical properties of (001) oriented β -(Al_xGa_{1-x})₂O₃ films for all investigated Al compositions. However, further investigation beyond the scope of this work is necessary to fully understand the n-type doping in (001) β -(Al_xGa_{1-x})₂O₃.

IV. Conclusion

In summary, the epitaxial growth of β -(Al_xGa_{1-x})₂O₃ thin films and β -(Al_xGa_{1-x})₂O₃/ β -Ga₂O₃ superlattice structures on (001) oriented β -Ga₂O₃ substrates are comprehensively investigated by MOCVD. The structural, chemical, and surface morphological properties of β -(Al_xGa_{1-x})₂O₃ films with different Al compositions, including Al incorporation, strain, surface RMS roughness, alloy homogeneity, bandgap and band offsets are investigated by extensive material characterizations. XRD, STEM EDX elemental mapping, and APT measurements show up to 25% Al incorporation in coherently strained β -(Al_xGa_{1-x})₂O₃ thin films grown along (001) orientation. Although smooth surface morphologies are observed, chemical inhomogeneity with directional dependence of Al distribution along ($\bar{2}01$) primary cleavage plane is observed in the films. The determined band offsets at β -(Al_xGa_{1-x})₂O₃/ β -Ga₂O₃ interfaces with different Al

compositions reveal the formation of type-II band alignment. The n-type conductivity is also investigated for different Al compositions. The results from this study on the epitaxial growth of (001) oriented β -(Al_xGa_{1-x})₂O₃ alloys is promising for the development of future high power and high frequency electronic and optoelectronic devices based on β -(Al_xGa_{1-x})₂O₃/ β -Ga₂O₃ heterostructure.

Acknowledgements

The authors acknowledge the Air Force Office of Scientific Research FA9550-18-1-0479 (AFOSR, Dr. Ali Sayir) for financial support. The electron microscopy was performed at the Center for Electron Microscopy and Analysis (CEMAS) at The Ohio State University. The authors also acknowledge the National Science Foundation (Grant No. 2231026, No. 2019753) and Semiconductor Research Corporation (SRC) under the Task ID GRC 3007.001 for partial support.

Data Availability

The data that support the findings of this study are available from the corresponding author upon reasonable request.

References

1. H. Peelaers, J. B. Varley, J. S. Speck, and C. G. Van de Walle, *Appl. Phys. Lett.* 112, 242101 (2018).
2. J. B. Varley, *J. Mater. Res.* 36, 4790 (2021).
3. J. B. Varley, A. Perron, V. Lordi, D. Wickramaratne, and J. L. Lyons, *Appl. Phys. Lett.* 116, 172104 (2020).
4. K. Ghosh and U. Singiseti, *J. Mater. Res.* 32, 4142 (2017).
5. S. Krishnamoorthy, Z. Xia, C. Joishi, Y. Zhang, J. McGlone, J. Johnson, M. Brenner, A. R. Arehart, J. Hwang, S. Lodha, and S. Rajan, *Appl. Phys. Lett.* 111, 023502 (2017).
6. A. Kumara, K. Ghosh, and U. Singiseti, *J. Appl. Phys.* 128, 105703 (2020).
7. Y. Zhang, A. Neal, Z. Xia, C. Joishi, J. M. Johnson, Y. Zheng, S. Bajaj, M. Brenner, D. Dorsey, K. Chabak, G. Jessen, J. Hwang, S. Mou, J. P. Heremans, and S. Rajan, *Appl. Phys. Lett.* 112, 173502 (2018).

8. P. Ranga, A. Bhattacharyya, A. Chmielewski, S. Roy, R. Sun, M. A. Scarpulla, N. Alem, and S. Krishnamoorthy, *Appl. Phys. Express* 14, 025501 (2021).
9. A F M A. U. Bhuiyan, Z. Feng, J. M. Johnson, Z. Chen, H.-L. Huang, J. Hwang, and H. Zhao, *Appl. Phys. Lett.* 115, 120602 (2019).
10. A F M A. U. Bhuiyan, Z. Feng, L. Meng, A. Fiedler, H.-L. Huang, A. T. Neal, E. Steinbrunner, S. Mou, J. Hwang, S. Rajan and H. Zhao, *J. Appl. Phys.* 131, 145301 (2022).
11. A F M A. U. Bhuiyan, Z. Feng, L. Meng, H. Zhao, *J. Mater. Res.* 36, 4804 (2021).
12. S. W. Kaun, F. Wu, and J. S. Speck, *J. Vac. Sci. Technol. A* 33, 041508 (2015).
13. A F M A. U. Bhuiyan, Z. Feng, J. M. Johnson, H.-L. Huang, J. Sarker, M. Zhu, M. R. Karim, B. Mazumder, J. Hwang, and H. Zhao, *APL Mater.* 8, 031104 (2020).
14. J. M. Johnson, H.-L. Huang, M. Wang, S. Mu, J. B. Varley, A. F. M. A. U. Bhuiyan, Z. Feng, N. K. Kalarickal, S. Rajan, H. Zhao, C. G. Van de Walle, and J. Hwang, *APL Materials* 9, 051103 (2021).
15. A F M A. U. Bhuiyan, Z. Feng, J. M. Johnson, H.-L. Huang, J. Sarker, M. Zhu, M. R. Karim, B. Mazumder, J. Hwang, and H. Zhao, *APL Materials* 8 (8), 089102 (2020).
16. J. Sarker, A. F. M. A. U. Bhuiyan, Z. Feng, H. Zhao and B. Mazumder, *J. Phys. D: Appl. Phys.* 54, 184001 (2021).
17. J. Sarker, S. Broderick, A. F. M. A. U. Bhuiyan, Z. Feng, H. Zhao, and B. Mazumder, *Appl. Phys. Lett.* 116, 152101 (2020).
18. A F M A. U. Bhuiyan, Z. Feng, J. M. Johnson, H.-L. Huang, J. Hwang, and H. Zhao, *Cryst. Growth Des.* 20, 6722 (2020).
19. A F M A. U. Bhuiyan, Z. Feng, J. M. Johnson, H.-L. Huang, J. Hwang, and H. Zhao, *Appl. Phys. Lett.* 117, 142107 (2020).
20. A F M A. U. Bhuiyan, Z. Feng, J. M. Johnson, H.-L. Huang, J. Hwang, and H. Zhao, *Appl. Phys. Lett.* 117, 252105 (2020).
21. A F M A. U. Bhuiyan, Z. Feng, H.-L. Huang, L. Meng, J. Hwang, H. Zhao, *J. Vac. Sci. Technol. A* 39, 063207 (2021).
22. Z. Hu, H. Zhou, Q. Feng, J. Zhang, C. Zhang, K. Dang, Y. Cai, Z. Feng, Y. Gao, X. Kang, and Y. Hao, *IEEE Electron Device Lett.* 39, 1564-1567 (2018).
23. W. Li, K. Nomoto, Z. Hu, D. Jena, and H. G. Xing, *IEEE Electron Device Lett.* 41, 107-110 (2020).
24. K. Konishi, K. Goto, H. Murakami, Y. Kumagai, A. Kuramata, S. Yamakoshi, and M. Higashiwaki, *Appl. Phys. Lett.* 110, 103506 (2017).
25. K. Sasaki, D. Wakimoto, Q. T. Thieu, Y. Koishikawa, A. Kuramata, M. Higashiwaki, and S. Yamakoshi, *IEEE Electron Device Lett.* 38, 783 (2017).
26. Q. Yan, H. Gong, J. Zhang, J. Ye, H. Zhou, Z. Liu, S. Xu, C. Wang, Z. Hu, Q. Feng, J. Ning, C. Zhang, P. Ma, R. Zhang, and Y. Hao, *Appl. Phys. Lett.* 118, 122102 (2021).

27. W. Li, K. Nomoto, Z. Hu, N. Tanen, K. Sasaki, A. Kuramata, D. Jena and H. G. Xing, 1.5 kV Vertical Ga₂O₃ Trench-MIS Schottky Barrier Diodes, 2018 76th Device Research Conference (DRC), 2018, pp. 1-2, doi: 10.1109/DRC.2018.8442245.
28. A. Mauze, T. Itoh, Y. Zhang, E. Deagueros, F. Wu, and J. S. Speck, *J. Appl. Phys.* 132, 115302 (2022).
29. M. K. Miller, K. F. Russell, K. Thompson, R. Alvis and D. J. Larson, *Microsc. Microanal.* 13, 428 (2007).
30. K. Kaneko, K. Suzuki, Y. Ito, and S. Fujita, *J. Cryst. Growth*, 436, 150 (2016).
31. F. A. Cotton, *Chemical Applications of Group Theory*, 2nd ed., Wiley-Interscience, New York, 1971.
32. T. Onuma, S. Fujioka, T. Yamaguchi, Y. Itoh, M. Higashiwaki, K. Sasaki, T. Masui, T. Honda, *J. Cryst. Growth* 401, 330 (2014).
33. C. Kranert, C. Sturm, R. Schmidt-Grund, and M. Grundmann. *Sci Rep* 6, 35964 (2016).
34. D. Dohy, G. Lucazeau, and A. Revcolevschi, *J. Solid State Chem.* 45 180 (1982).
35. S. Mu, M. Wang, H. Peelaers, and C. G. Van de Walle, *APL Mater.* 8, 091105 (2020).
36. B. Mazumder, J. Sarker, Y. Zhang, J. M. Johnson, M. Zhu, S. Rajan, and J. Hwang, *Appl. Phys. Lett.* 115, 132105 (2019).
37. Y. R. Luo, Bond Dissociation Energies. In *CRC Handbook of Chemistry and Physics*, 90th ed.; Lide, D. R., Ed.; CRC Press/Taylor and Francis,: Boca Raton, FL, 2009
38. A. Devaraj, M. Gu, R. Colby, P. Yan, C. M. Wang, J. M. Zheng, J. Xiao, A. Genc, J. G. Zhang, I. Belharouak, D. Wang, K. Amine, and S. Thevuthasan, *Nat. Commun.* 6, 8014 (2015).
39. M. T. Nichols, W. Li, D. Pei, G. A. Antonelli, Q. Lin, S. Banna, Y. Nishi, and J. L. Shohet, *J. Appl. Phys.* 115, 094105 (2014).
40. A F M A. U. Bhuiyan, Z. Feng, H.-L. Huang, L. Meng, J. Hwang, H. Zhao, *APL Mater.* 9, 101109 (2021).
41. A F M A. U. Bhuiyan, Z. Feng, H.-L. Huang, L. Meng, J. Hwang, H. Zhao, *J. Vac. Sci. Technol. A* 40, 062704 (2022).
42. A F M A. U. Bhuiyan, L. Meng, H.-L. Huang, J. Hwang, H. Zhao, *J. Appl. Phys.* 132, 165301 (2022).
43. E. A. Kraut, R. W. Grant, J. R. Waldrop, and S. P. Kowalczyk, *Phys. Rev. Lett.* 44, 1620 (1980).
44. S. Mu, H. Peelaers, Y. Zhang, M. Wang, and C. G. Van de Walle, *Appl. Phys. Lett.* 117, 252104 (2020).

Figure Captions

Figure 1. XRD ω - 2θ scan profiles of the (002) reflections of β -(Al_xGa_{1-x})₂O₃ films grown on (001) β -Ga₂O₃ substrates with Al incorporations of (a) 11%, (b) 14% and (c) 25%. Asymmetrical reciprocal space maps (RSMs) around ($\bar{2}$ 04) reflections of (001) β -(Al_xGa_{1-x})₂O₃ films with (d) $x = 11\%$, (e) $x = 14\%$, and (f) $x = 25\%$. The vertical and tilted white dashed line represent fully strained and fully relaxed positions, respectively.

Figure 2. (a) Surface view FESEM and (b) AFM images of β -(Al_xGa_{1-x})₂O₃ films with 14% Al compositions.

Figure 3. Room-temperature Raman spectra of β -(Al_xGa_{1-x})₂O₃ films with Al compositions of 11%, 14% and 25%. The Raman spectra from (001) β -Ga₂O₃ bare substrate is also included.

Figure 4. Atomic resolution cross-sectional HAADF-STEM images of β -(Al_xGa_{1-x})₂O₃ film with 14% Al compositions at (a) 50 nm and (b) 5 nm scales, showing Al distribution pattern along ($\bar{2}$ 01) cleavage plane with ~ 17 nm thick homogenous and uniform β -(Al_xGa_{1-x})₂O₃ layer at the interface. The HAADF-STEM images were taken from the $\langle 010 \rangle$ zone axes.

Figure 5. STEM-EDX mapping of β -(Al_xGa_{1-x})₂O₃ film with 14% Al compositions. (a) Cross-sectional HAADF image with corresponding EDX mapping of (b) Ga, (c) Al and (d) O atoms. (e) Atomic fraction elemental profile as indicated by the orange arrow in (a).

Figure 6. STEM-EDX mapping of β -(Al_xGa_{1-x})₂O₃ film with 14% Al compositions, showing tilted Al distribution region (a) Cross-sectional HAADF image with corresponding EDX mapping of (b) Ga, (c) Al and (d) O atoms. (e) Atomic fraction elemental profile as indicated by the orange arrow in (a).

Figure 7. STEM-EDX mapping of $\beta\text{-(Al}_x\text{Ga}_{1-x})_2\text{O}_3$ film with 14% Al compositions, showing uniform Al distribution region at the interface (a) Cross-sectional HAADF image with corresponding EDX mapping of (b) Ga, (c) Al and (d) O atoms. (e) Atomic fraction elemental profile along the orange arrow in (a).

Figure 8. High resolution cross-sectional HAADF-STEM images of 8 period (001) $\beta\text{-(Al}_x\text{Ga}_{1-x})_2\text{O}_3/\beta\text{-Ga}_2\text{O}_3$ superlattice structure grown with targeted Al composition of 14% in $\beta\text{-(Al}_x\text{Ga}_{1-x})_2\text{O}_3$ layer at (a) 100 nm and (b) 20 nm scales, showing wavy and inhomogeneous interfaces between $\beta\text{-(Al}_x\text{Ga}_{1-x})_2\text{O}_3$ and $\beta\text{-Ga}_2\text{O}_3$ layers. The HAADF-STEM images were taken from the $\langle 010 \rangle$ zone axes.

Figure 9. STEM-EDX mapping of (001) $\beta\text{-(Al}_x\text{Ga}_{1-x})_2\text{O}_3/\beta\text{-Ga}_2\text{O}_3$ superlattice structure grown with targeted Al compositions of 14% (a) Cross-sectional HAADF image with corresponding EDX mapping of (b) Ga, (c) Al and (d) O atoms. (e) Atomic fraction elemental profile along the orange arrow in (a), showing 8 periods of the SL structure.

Figure 10. (a) Schematic of (001) $\beta\text{-(Al}_x\text{Ga}_{1-x})_2\text{O}_3/\beta\text{-Ga}_2\text{O}_3$ heterostructures with varying TMAI flow rates analyzed in APT. (b) A 3D atom map of the corresponding structure, only Al and Ga atoms are shown for clarity in red and blue, respectively. (c) Elemental (III-site) composition profile of the analyzed heterostructure in (a).

Figure 11. (a)-(f) In-plane Al/Ga distributions for each (001) $\beta\text{-(Al}_x\text{Ga}_{1-x})_2\text{O}_3$ layer grown with TMAI flow rates of 1–6 SCCM, respectively.

Figure 12. (a)-(f) Frequency distribution analysis of Al in $\beta\text{-(Al}_x\text{Ga}_{1-x})_2\text{O}_3$ layers grown with TMAI flow rates of 1- 6 SCCM, respectively.

Figure 13. Ga $2p_{3/2}$ core level spectra of (001) oriented $\beta\text{-(Al}_x\text{Ga}_{1-x})_2\text{O}_3$ film for $x = 25\%$ with the peak position located at 1117.85 eV binding energy. The inset shows the zoomed view of the

inelastic background region. The bandgap of 5.15 ± 0.15 eV is calculated from the difference between the position of Ga $2p_{3/2}$ core-level and the onset of the inelastic background.

Figure 14. Ga 3d and Al 2p core-levels and valence band (VB) spectra from (a) 50 nm thick (001) β -Ga₂O₃ film (b) 200 nm thick β -(Al_xGa_{1-x})₂O₃ film and (c) β -(Al_xGa_{1-x})₂O₃/ β -Ga₂O₃ (2 nm/65 nm) interface with $x = 25\%$. Experimental data points are shown as black open circles and the fitted curves are represented as black dashed lines. Blue solid straight lines in (b) and (d) represent the linear fitting of VB spectra of β -Ga₂O₃ and β -(Al_xGa_{1-x})₂O₃ films, respectively.

Figure 15. Conduction band offsets at β -(Al_xGa_{1-x})₂O₃/ β -Ga₂O₃ interfaces as a function of Al composition for (010), (100), ($\bar{2}$ 01) and (001) orientations. The dotted lines represent the theoretical predictions of the conduction band offsets for different orientations.

Figure 16. Room temperature Hall mobility vs. carrier concentration for β -(Al_xGa_{1-x})₂O₃ films grown on (001) oriented β -(Al_xGa_{1-x})₂O₃ substrates with various Al compositions.

Table 1.

Summary of the valance and conduction band offsets at (001) β -(Al_{0.25}Ga_{0.75})₂O₃/ β -Ga₂O₃ interfaces, estimated by using valance band maximum, Ga 3d and Al 2p core levels and VBM positions from XPS measurement.

Al compositi on	Bandgap energy (eV) (± 0.15 eV)	(E _{Ga 3d} ^{GaO})	(E _{Al 2p} ^{AlGaO})	(E _{Ga 3d} ^{AlGaO/GaO})	ΔE_v (eV) (± 0.06 eV)	ΔE_c (eV) (± 0.22 eV)
		- E _{VBM} ^{GaO} (eV) (± 0.04 eV)	- E _{VBM} ^{AlGaO} (eV) (± 0.04 eV)	- E _{Al 2p} ^{AlGaO/GaO} (eV) (± 0.02 eV)		
0%	4.88	16.89				
11%	5.04		71.00	-54.07	-0.04	0.17
25%	5.15		71.14	-54.17	-0.08	0.35

Figure 1

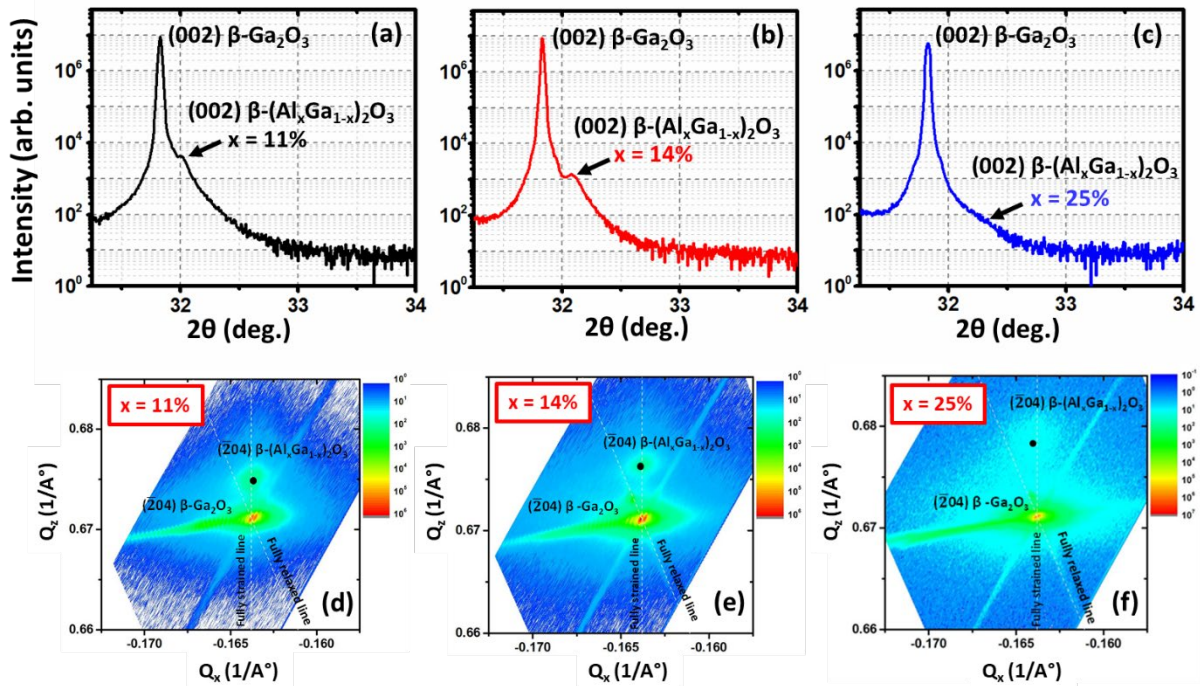


Figure 1. XRD ω - 2θ scan profiles of the (002) reflections of β - $(\text{Al}_x\text{Ga}_{1-x})_2\text{O}_3$ films grown on (001) β - Ga_2O_3 substrates with Al incorporations of (a) 11%, (b) 14% and (c) 25%. Asymmetrical reciprocal space maps (RSMs) around $(\bar{2}04)$ reflections of (001) β - $(\text{Al}_x\text{Ga}_{1-x})_2\text{O}_3$ films with (d) $x = 11\%$, (e) $x = 14\%$, and (f) $x = 25\%$. The vertical and tilted white dashed line represent fully strained and fully relaxed positions, respectively.

Figure 2

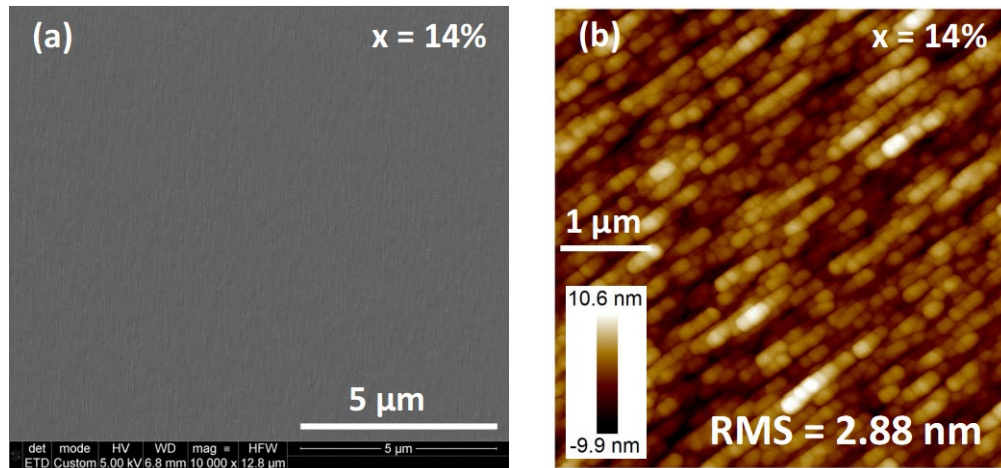


Figure 2. (a) Surface view FESEM and (b) AFM images of β -(Al_xGa_{1-x})₂O₃ films with 14% Al compositions.

Figure 3

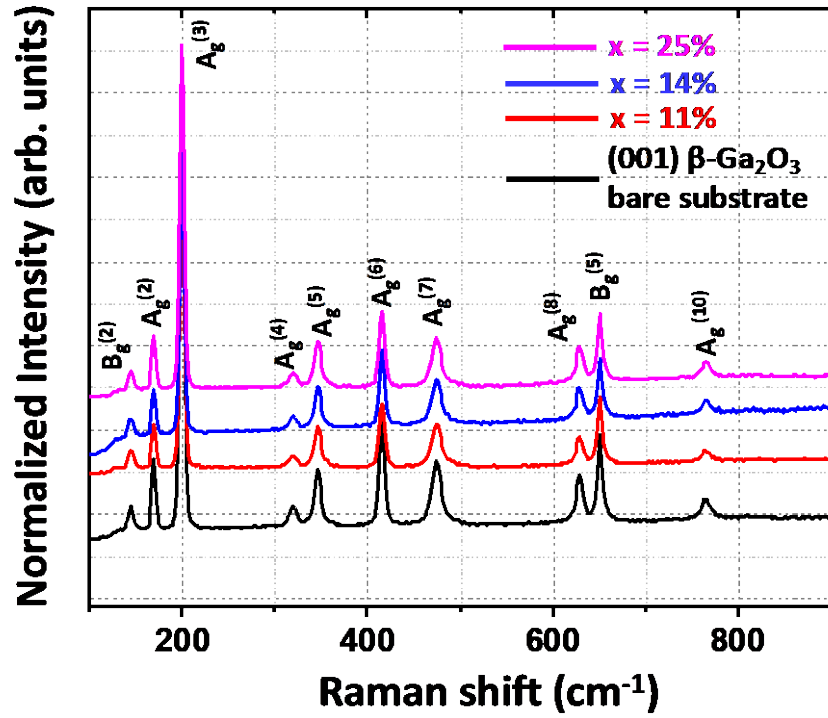


Figure 3. Room-temperature Raman spectra of β -(Al_xGa_{1-x})₂O₃ films with Al compositions of 11%, 14% and 25%. The Raman spectra from (001) β -Ga₂O₃ bare substrate is also included.

Figure 4

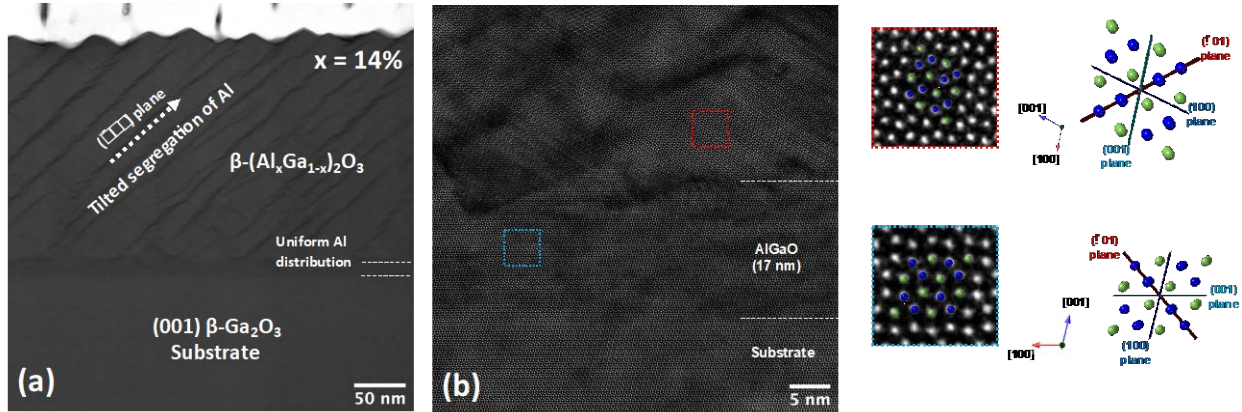


Figure 4. Atomic resolution cross-sectional HAADF-STEM images of β - $(\text{Al}_x\text{Ga}_{1-x})_2\text{O}_3$ film with 14% Al compositions at (a) 50 nm and (b) 5 nm scales, showing Al distribution pattern along $(\bar{2}01)$ cleavage plane with ~ 17 nm thick homogenous and uniform β - $(\text{Al}_x\text{Ga}_{1-x})_2\text{O}_3$ layer at the interface. The HAADF-STEM images were taken from the $\langle 010 \rangle$ zone axes.

Figure 5

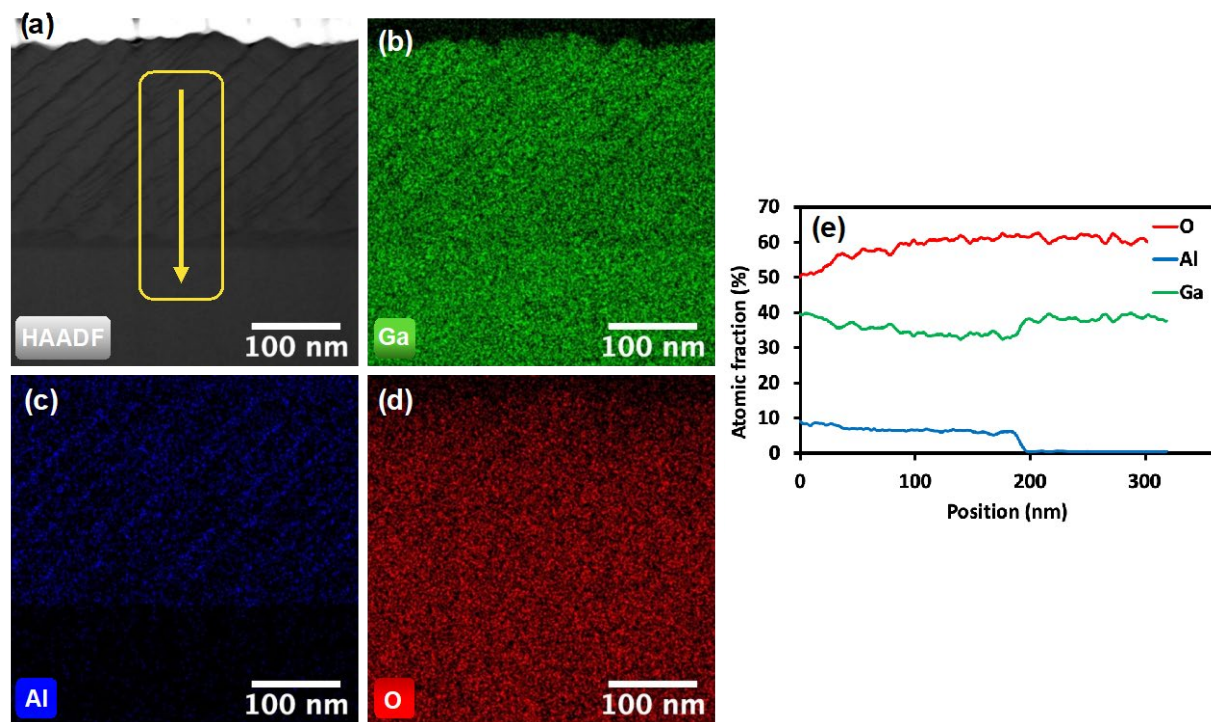


Figure 5. STEM-EDX mapping of β -($\text{Al}_x\text{Ga}_{1-x}$) $_2\text{O}_3$ film with 14% Al compositions. (a) Cross-sectional HAADF image with corresponding EDX mapping of (b) Ga, (c) Al and (d) O atoms. (e) Atomic fraction elemental profile as indicated by the orange arrow in (a).

Figure 6

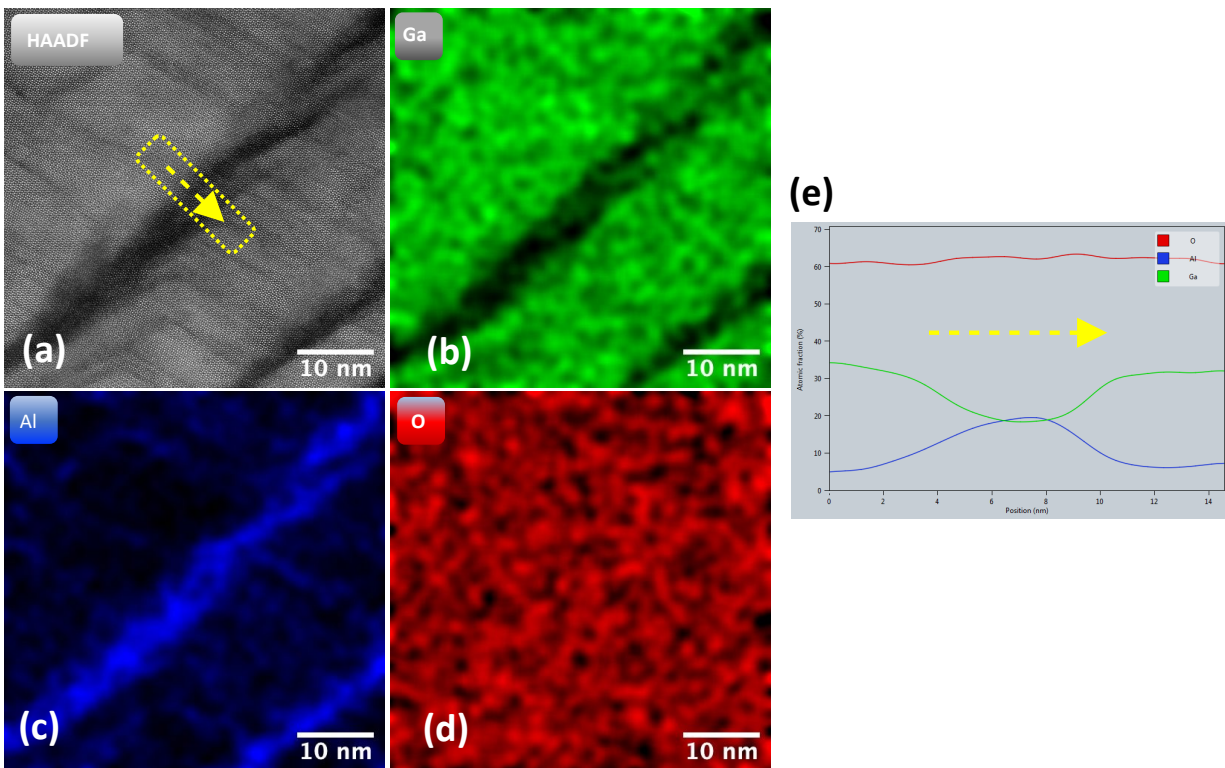


Figure 6. STEM-EDX mapping of β -($\text{Al}_x\text{Ga}_{1-x}$) $_2\text{O}_3$ film with 14% Al compositions, showing tilted Al distribution region (a) Cross-sectional HAADF image with corresponding EDX mapping of (b) Ga, (c) Al and (d) O atoms. (e) Atomic fraction elemental profile as indicated by the orange arrow in (a).

Figure 7

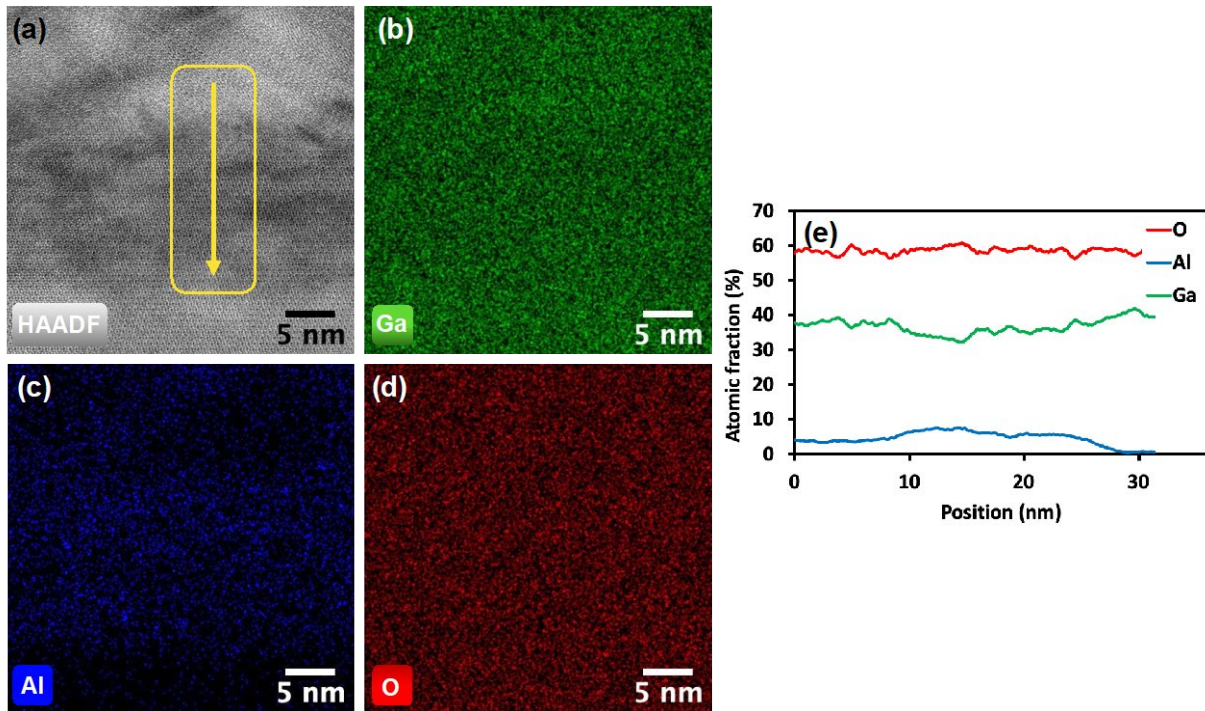


Figure 7. STEM-EDX mapping of β -(Al_xGa_{1-x})₂O₃ film with 14% Al compositions, showing uniform Al distribution region at the interface (a) Cross-sectional HAADF image with corresponding EDX mapping of (b) Ga, (c) Al and (d) O atoms. (e) Atomic fraction elemental profile along the orange arrow in (a).

Figure 8

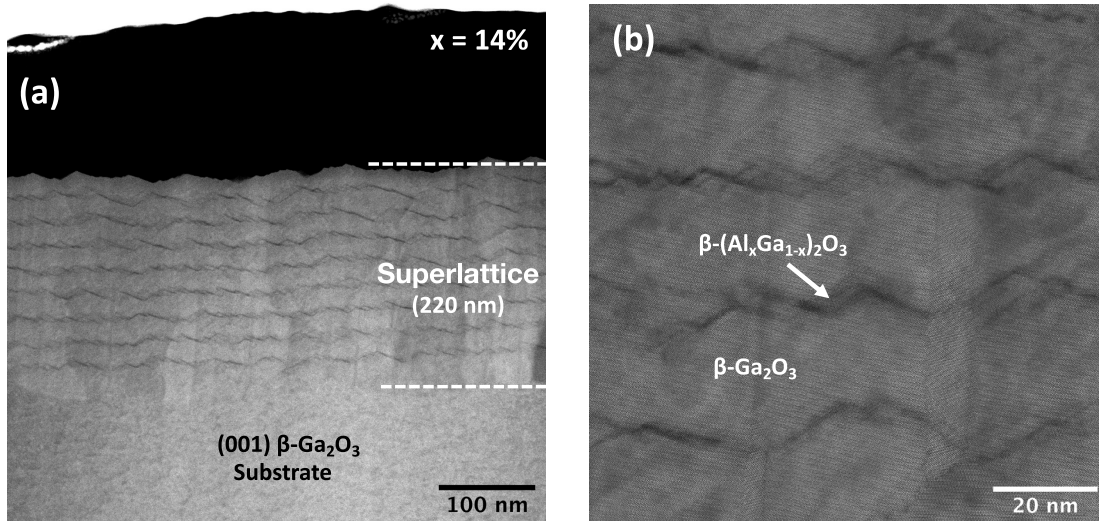


Figure 8. High resolution cross-sectional HAADF-STEM images of 8 period β -(Al_xGa_{1-x})₂O₃/β-Ga₂O₃ superlattice structure grown with targeted Al composition of 14% in β-(Al_xGa_{1-x})₂O₃ layer at (a) 100 nm and (b) 20 nm scales, showing wavy and inhomogeneous interfaces between β-(Al_xGa_{1-x})₂O₃ and β-Ga₂O₃ layers. The HAADF-STEM images were taken from the $\langle 010 \rangle$ zone axes.

Figure 9

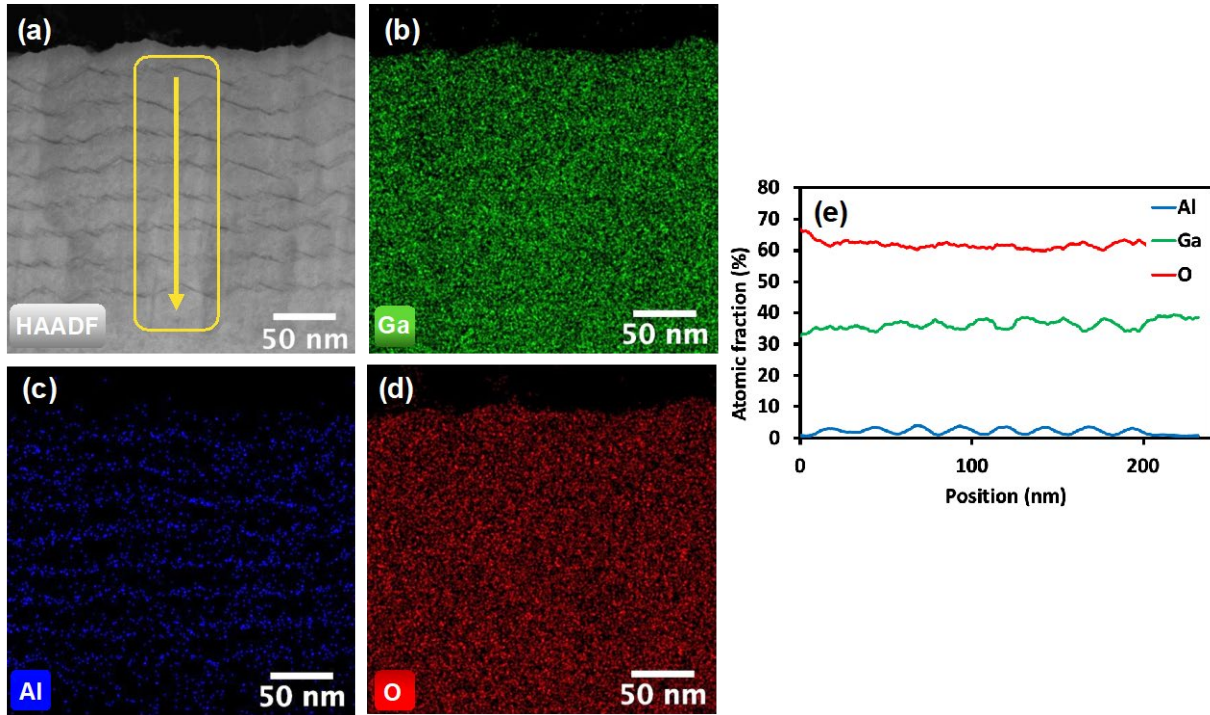


Figure 9. STEM-EDX mapping of (001) β -($\text{Al}_x\text{Ga}_{1-x}$) $_2\text{O}_3/\beta$ - Ga_2O_3 superlattice structure grown with targeted Al compositions of 14% (a) Cross-sectional HAADF image with corresponding EDX mapping of (b) Ga, (c) Al and (d) O atoms. (e) Atomic fraction elemental profile along the orange arrow in (a), showing 8 periods of the SL structure.

Figure 10

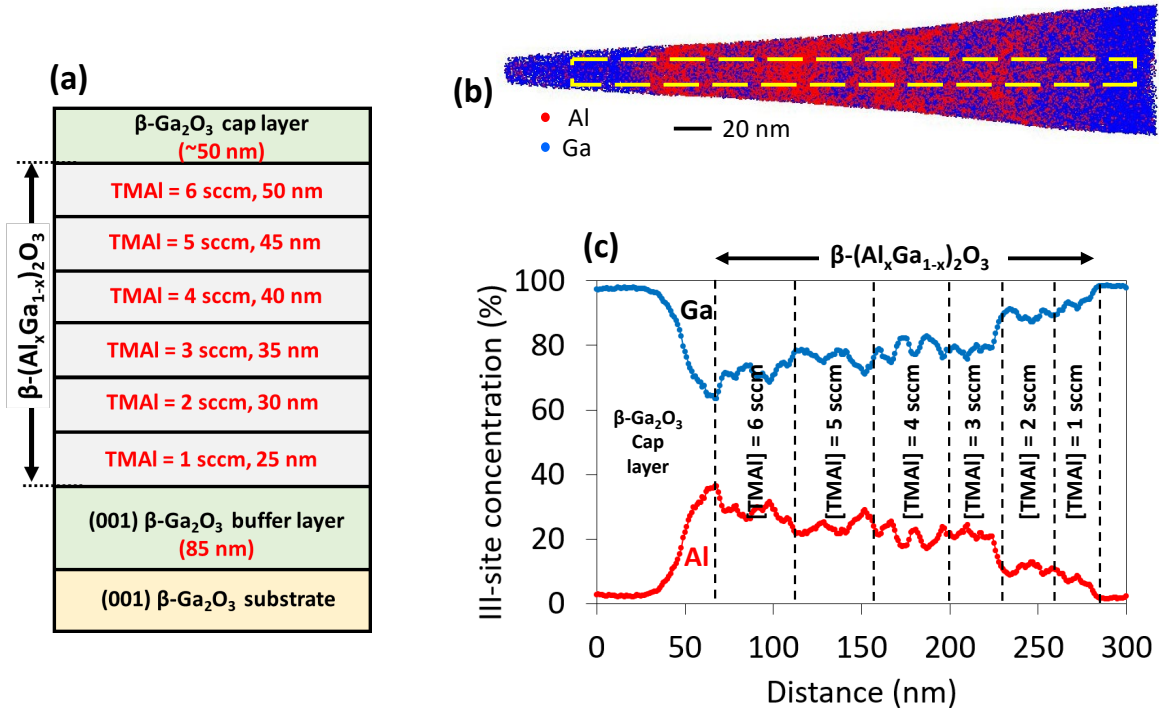


Figure 10. (a) Schematic of (001) $\beta\text{-(Al}_x\text{Ga}_{1-x})_2\text{O}_3/\beta\text{-Ga}_2\text{O}_3$ heterostructures with varying TMAI flow rates analyzed in APT. (b) A 3D atom map of the corresponding structure, only Al and Ga atoms are shown for clarity in red and blue, respectively. (c) Elemental (III-site) composition profile of the analyzed heterostructure in (a).

Figure 11

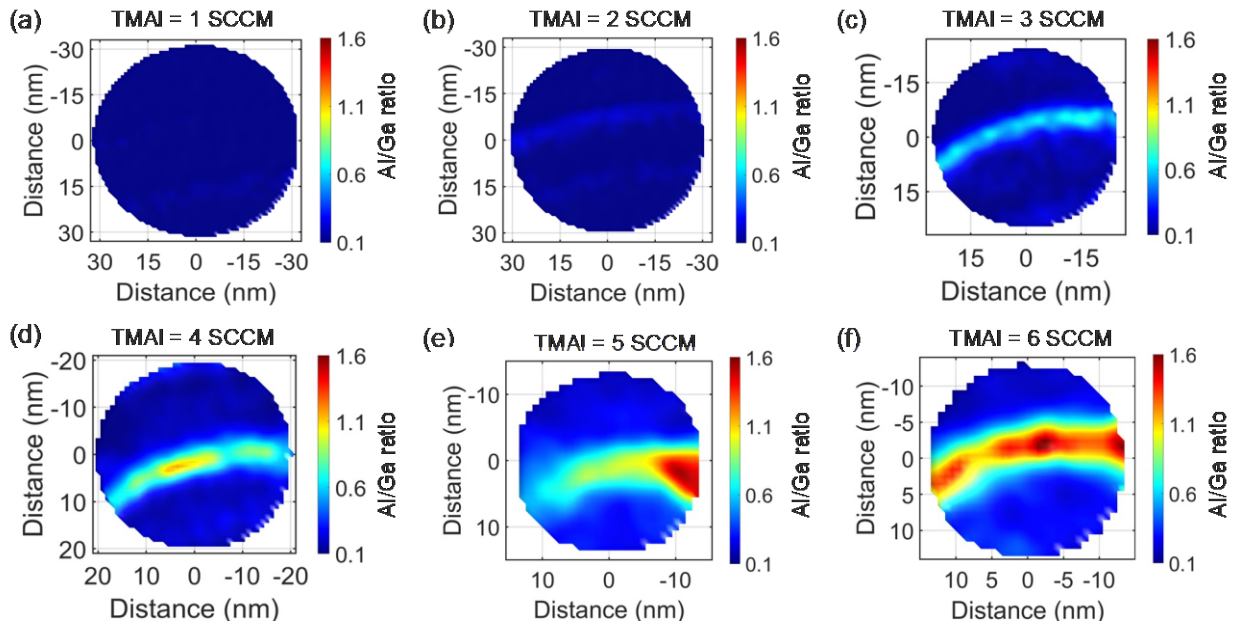


Figure 11. (a)-(f) In-plane Al/Ga distributions for each (001) β - $(\text{Al}_x\text{Ga}_{1-x})_2\text{O}_3$ layer grown with TMAI flow rates of 1–6 SCCM, respectively.

Figure 12

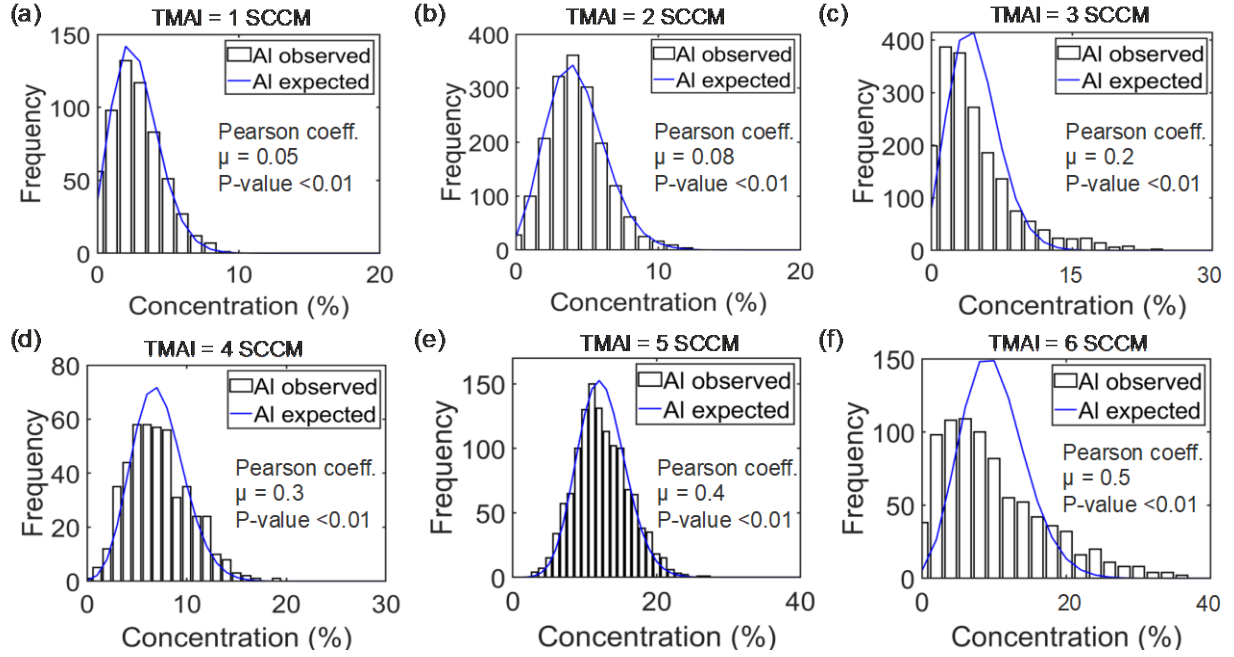


Figure 12. (a)-(f) Frequency distribution analysis of Al in β -(Al_xGa_{1-x})₂O₃ layers grown with TMAI flow rates of 1- 6 SCCM, respectively.

Figure 13

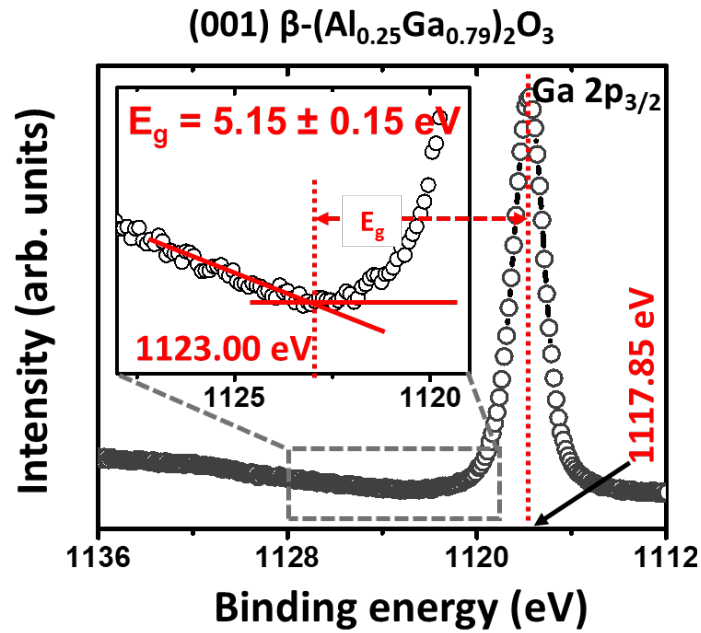


Figure 13. Ga 2p_{3/2} core level spectra of (001) oriented β -(Al_xGa_{1-x})₂O₃ film for x = 25% with the peak position located at 1117.85 eV binding energy. The inset shows the zoomed view of the inelastic background region. The bandgap of 5.15 ± 0.15 eV is calculated from the difference between the position of Ga 2p_{3/2} core-level and the onset of the inelastic background.

Figure 14

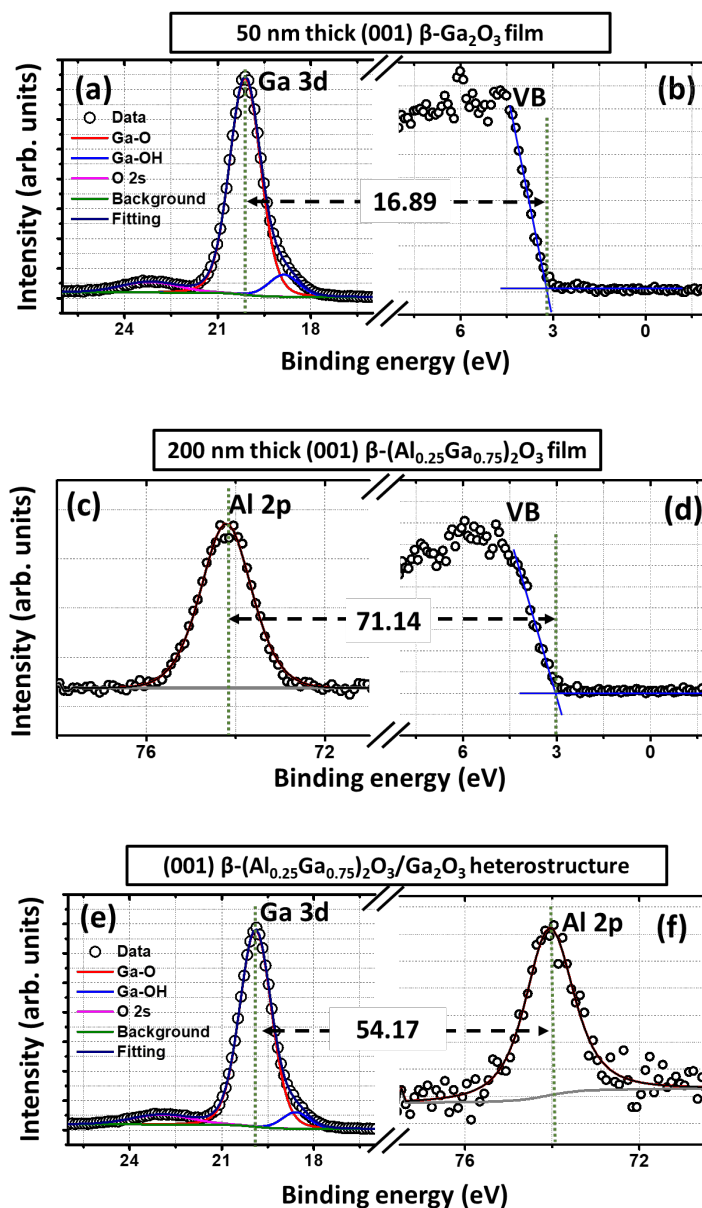


Figure 14. Ga 3d and Al 2p core-levels and valence band (VB) spectra from (a) 50 nm thick (001) β -Ga₂O₃ film (b) 200 nm thick β -(Al_xGa_{1-x})₂O₃ film and (c) β -(Al_xGa_{1-x})₂O₃/ β -Ga₂O₃ (2 nm/65 nm) interface with $x = 25\%$. Experimental data points are shown as black open circles and the fitted curves are represented as black dashed lines. Blue solid straight lines in (b) and (d) represent the linear fitting of VB spectra of β -Ga₂O₃ and β -(Al_xGa_{1-x})₂O₃ films, respectively.

Figure 15

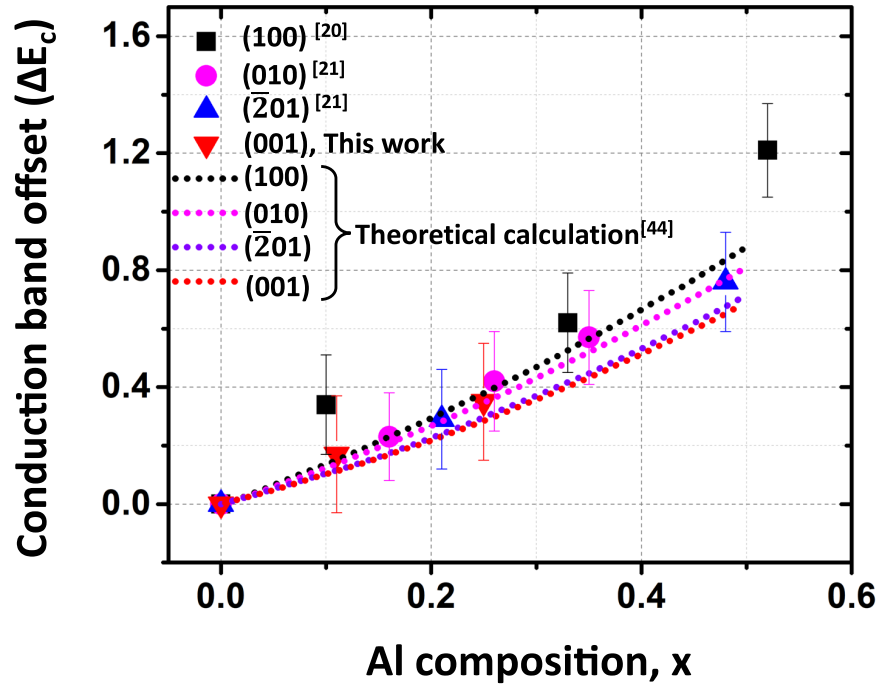


Figure 15. Conduction band offsets at β - $(\text{Al}_x\text{Ga}_{1-x})_2\text{O}_3/\beta$ - Ga_2O_3 interfaces as a function of Al composition for (010), (100), $(\bar{2}01)$ and (001) orientations. The dotted lines represent the theoretical predictions of the conduction band offsets for different orientations.

Figure 16

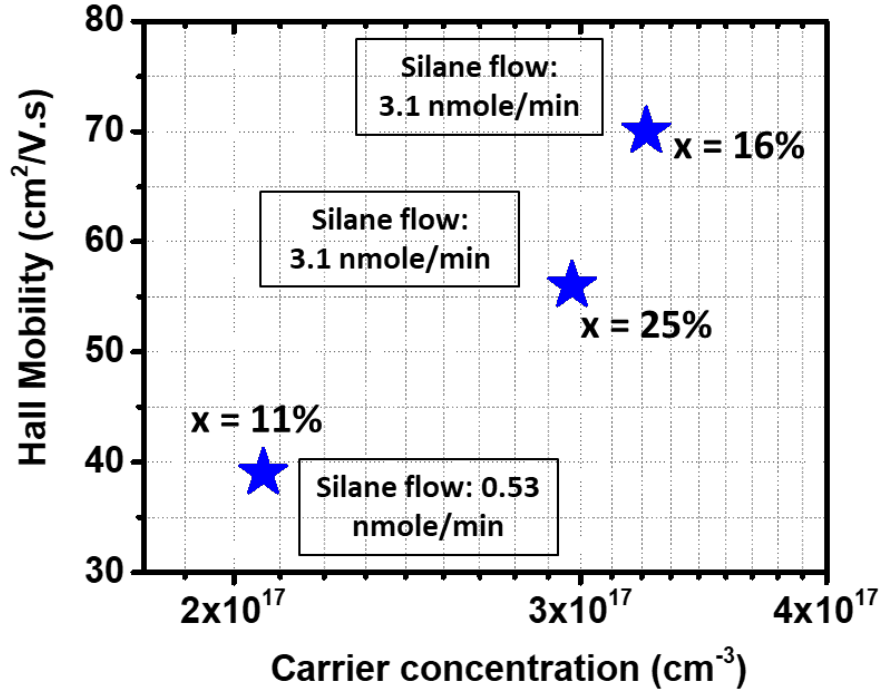


Figure 16. Room temperature Hall mobility vs. carrier concentration for β -(Al_xGa_{1-x})₂O₃ films grown on (001) oriented β -(Al_xGa_{1-x})₂O₃ substrates with various Al compositions.